Modeling of Ni–CGO anode in a solid oxide fuel cell deposited by spray pyrolysis

Lin Liu, Gap-Yong Kim*, Abhijit Chandra

Department of Mechanical Engineering, Iowa State University, Ames, IA, USA

ABSTRACT

A complete electrode polarization model of a solid oxide fuel cell (SOFC) has been developed and utilized to analyze the performance of Ni–CGO anode deposited by spray pyrolysis. The model integrated a macro model and a micro model to consider electrode microstructural parameters in overall cell behavior. Three different microstructures were prepared by varying the processing conditions. The model was capable of predicting the electrochemical performance of the different microstructural variations with discrepancy smaller than 10%. It was found that the activation loss was most dominant of all three major voltage losses. The decrease in particle size improved the anode performance due to the increase in triple phase boundary area. The model also showed that optimal particle size decreased with increasing anode porosity. Overall, the work contributed to the understanding of cell performance in relation to the anode electrode microstructure.

© 2012 Elsevier B.V. All rights reserved.

1. Introduction

Solid oxide fuel cell (SOFC) is an environmentally friendly technology that has the potential to meet the critical energy needs of our modern civilization with minimal adverse environmental impact from excessive energy consumption. They are highly efficient, clean and can run on variety of fuel gases [1–6]. Current research is much focused on reducing the manufacturing cost, improving the cell efficiency, and enhancing the cell life in the SOFC system [7–11]. One potential way to improve cell performance is to manipulate the cell microstructure. SOFC electrode electrochemical behavior is mainly determined by three major losses: activation loss, Ohmic loss, and concentration loss. These values are significantly influenced by the microstructure of the electrode [12,13]. Reaction and concentration losses depend on the quantity and location of the triple phase boundary (TPB), where a reactant gas molecule, an electronic conductor, and an ionic conductor join to convert fuel's chemical energy to electrical energy [14], as shown in Fig. 1. Previous investigations have explored improving SOFC electrochemical performance by controlling the electrode microstructure [15–22]. Ni et al. [15] presented a micro-scale model that was used to explore the performance of designed electrodes in SOFCs. Holtappels et al. [21] investigated SOFCs performance by controlling electrode porosity, which can optimize the gas transport in the substrate by maintaining a high

electrochemical activity for fuel oxidation at the anode–electrolyte interface. In our previous study, an experimental investigation on the effect of anode electrode microstructure on SOFC electrochemical performance was carried out [22]. In this study, a complete electrode polarization model of a SOFC has been developed and utilized to analyze the electrochemical performance of the SOFC with controlled microstructure. Both micro- and macro-scale kinetic and reaction mechanisms have been considered and integrated to complete the electrode performance evaluation. The developed model has been utilized to reveal the complex relationship between the transport phenomena and the electrochemical reaction at the TPB.

2. Model development

The previously developed electrode performance models account for the activation losses with the Butler–Volmer rate equation, conduction losses with Ohm's law, and concentration losses with combining a bulk gas diffusion theory with Knudsen diffusion. Greene et al. [23] investigated mass transfer losses in SOFCs with different porous electrodes using the mean transport pore model. One shortfall of the model was the parameter ψ, which was the porosity to tortuosity ratio. This does not allow for explicit input control of real porosity and tortuosity values. In addition, the activation losses were assumed to only occur at the electrode–electrolyte interface; however, this is generally not accepted to be true for a composite electrode [15]. Deseure et al. [24] and Schneider et al. [25] have modeled conduction percolation through electrodes. Deseure et al's model [24], however, did not account for varying reactant gas pressure through the electrode, which ignores the effect of concentration losses. Ni et al's model [15] was complete

* Corresponding author at: Iowa State University, Department of Mechanical Engineering, 2034 Black Engineering Building, Ames, IA 50011, USA.
Tel.: +1 515 294 6938; fax: +1 515 294 3261.
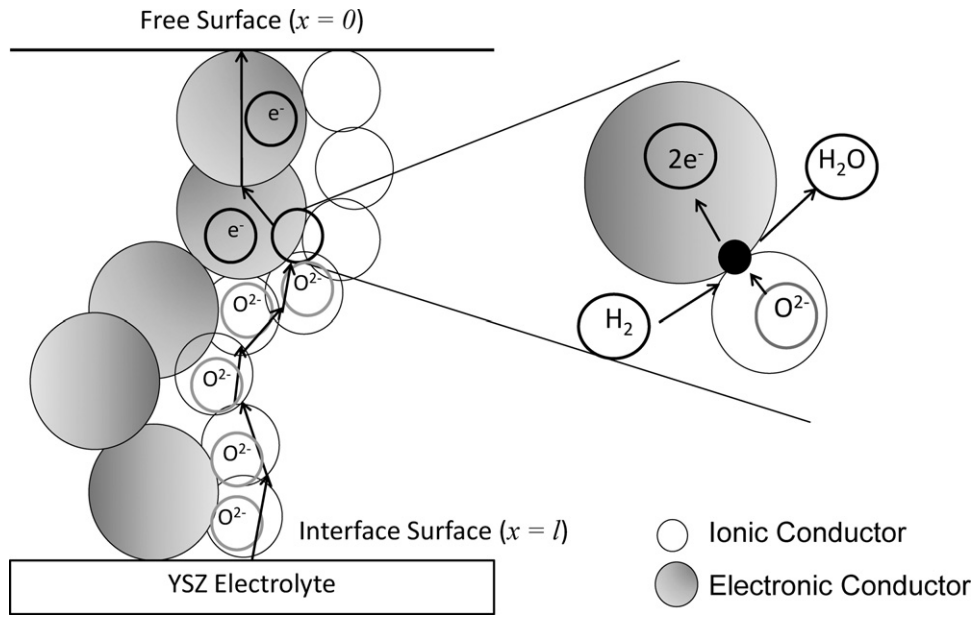*E-mail address:* gykim@iastate.edu (G.-Y. Kim).

Fig. 1. A schematic of TPB.

and varied the electrode microstructure, but this leaves many more verified structures to be explored.

In this work, a system behavior of particle- and porosity-varied SOFC electrode is studied by considering electrode behavior. This work expands upon previously developed theories and models [12,26]. The model consists of a macro and a micro model. The macro model describes the overall cell behavior through activation, Ohmic, and concentration losses based on chemical and concentration potentials. The micro model outputs effective resistivity of the porous electrode based on microstructural parameters such as pore diameter, particle size, and reaction area. The integration of macro and micro models is achieved by passing the micro model parameters to the macro model during the solution procedure.

In the macro model, the open circuit voltage (OCV), activation loss, Ohmic loss, and concentration (diffusion) losses are calculated. The operating cell voltage relationship can be expressed as:

$$V_{out} = V_{oc} - V_{loss} = V_{oc} - V_{ohm} - V_{act} - V_{conc} \tag{1}$$

where V_{out} is the output voltage; V_{oc} is the open circuit voltage; and V_{loss} is the total voltage loss. V_{loss} includes Ohmic loss voltage (V_{ohm}), activation loss voltage (V_{act}), and concentration loss voltage (V_{conc}).

The basic equations that are used in macro modeling are shared among many research papers [23,27,28]. The Nernst potential is used to calculate the open-circuit voltage of SOFCs:

$$V_{oc} = \frac{-\Delta g}{n_e F} + \frac{R_g T}{n_e F} \ln\left(\frac{p_{H_2}\sqrt{p_{O_2}}}{p_{H_2O}}\right) \tag{2}$$

where g is the Gibbs free energy; n_e is the number of electron in reaction; F is the Faraday's constant; R_g is the gas constant; T is the temperature; and p_A is the gas pressure of specie A.

In an electrochemical system, polarization is defined by the following equation [12,15,26]:

$$V_{loss} = (V_{el(eq)} - V_{io(eq)}) - (V_{el} - V_{io}) \tag{3}$$

where $V_{el(eq)}$ is the electronic equilibrium voltage; $V_{io(eq)}$ is the ionic equilibrium voltage; V_{el} is electronic voltage; and V_{io} is the ionic voltage.

The charge transport in an SOFC anode can be modeled based on the Ohm's law and the charge balance between the electronic and ionic conductors. The Ohm's law for electronic and ionic conductors are:

$$\frac{dV_{el}}{dx} = \rho_{el(eff)} i_{el} \quad \text{and} \quad \frac{dV_{io}}{dx} = \rho_{io(eff)} i_{io} \tag{4}$$

where $\rho_{el(eff)}$ is effective electronic resistivity; i_{el} is the electronic current density; $\rho_{io(eff)}$ is effective ionic resistivity; and i_{io} is the ionic current density. The charge balance in the electronic and ionic conductors is represented as:

$$\frac{di_{el}}{dx} = -\frac{di_{io}}{dx} = -A i_n \tag{5}$$

where i_n is the charge transfer current density; and A is the TPB given in the unit of area per volume. The Ohmic loss occurs due to the voltage gradient driving the charge transport and results in change of V_{loss}. Therefore, by combining Eqs. (3)–(5), the second derivative of Eq. (3) can be written as:

$$\frac{d^2 V_{loss}}{dx^2} = \rho_{io(eff)}\frac{di_{io}}{dx} - \rho_{el(eff)}\frac{di_{el}}{dx} = (\rho_{el(eff)} + \rho_{io(eff)})A i_n \tag{6}$$

Eq. (7) shows the Butler–Volmer equation which is commonly used to describe the activation polarization that occurs in a cell. The activation loss is caused by the potential needed for charge transfer and is dependent on reactant concentration, material, temperature, and surface properties. Butler–Volmer equation is a rate determining equation, which depends on the reaction mechanism. However, the exact reaction mechanism is difficult to identify because the formation of water may involve several intermediate steps. Other SOFC modeling work [29,30] verified the number of electron (n_e) transferred in the Butler–Volmer equation was one by comparing with experiments. The polarization model indicated that it was a one-electron transfer reaction mechanisms. Therefore, the reaction mechanism was simplified to assume each reaction occurrence is a one-step, single-electron transfer process [31].

$$i_n = i_o \left\{ \exp\left(\frac{\beta n_e F V_{act}}{R_g T}\right) - \exp\left(-(1-\beta)\frac{n_e F V_{act}}{R_g T}\right) \right\} \tag{7}$$
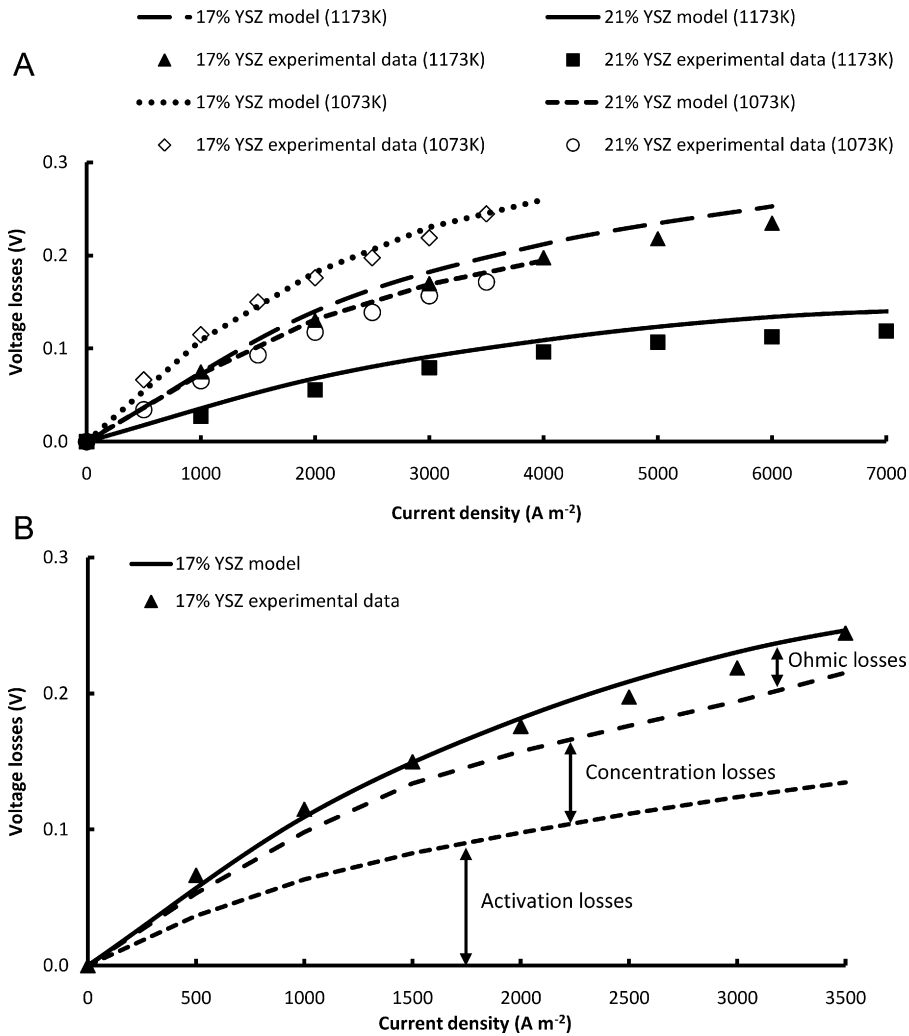
Fig. 2. Comparison between model simulation and experimental data of Jiang et al.: (a) voltage losses at 1073 K and 1173 K and (b) individual voltage losses at 1073 K.

where i_n is the charge transfer current density; i_o is the exchange current density; and β is the transfer coefficient (typically 0.5). Therefore, activation loss can be expressed as Eq. (8).

$$V_{\text{act}} = 2\frac{R_g T}{n_e F}\sinh^{-1}\left(\frac{i_n}{2i_o}\right) \qquad (8)$$

The concentration loss or mass transfer loss can be calculated from the Nernst potential difference between the bulk and TPB site:

$$V_{\text{conc}} = -\frac{R_g T}{n_e F}\ln\left(\frac{p_{r,H_2}\, p_{H_2O}^i}{p_{H_2}^i\, p_{r,H_2O}}\right) \qquad (9)$$

where $p_{H_2}^i$ is the inlet hydrogen pressure; p_{r,H_2} is the hydrogen pressure within the electrode; $p_{H_2O}^i$ is the inlet water vapor pressure; and p_{r,H_2} is the water vapor pressure within the electrode. The hydrogen and water pressures inside the electrode can be calculated by:

$$p_{r,H_2} = p_{H_2}^i - \frac{RTli_n}{n_e FD_{a(\text{eff})}} \quad \text{and} \quad p_{r,H_2O} = p_{H_2O}^i + \frac{RTli_n}{n_e FD_{a(\text{eff})}} \qquad (10)$$

where l is the anode thickness; and $D_{a(\text{eff})}$ is the anode effective diffusion coefficient.

Pressure gradient in the thickness direction can be obtained by combining the Fickian diffusion and current flux flowing in the electrode as the following:

$$\frac{dp_{H_2}}{dx} = -\frac{R_g T i_n}{2FD_{(\text{eff})}} \qquad (11)$$

where $D_{(\text{eff})}$ is the effective diffusion coefficient. This equation is valid for all depths throughout the electrode and can account for hydrogen consumption when combined with the Butler–Volmer equation.

$D_{(\text{eff})}$ can be found by considering binary and Knudsen diffusion models. Binary diffusion occurs where molecular–molecular interactions are dominant, and Knudsen diffusion occurs where molecular–surface interactions are dominant. The binary diffusion coefficient can be calculated with the Chapman–Enskog theory, as seen in Eqs. (12) and (13) [32]. σ_{AB} is the collision diameter and Ω_{DAB} is the collision integral based on the Lennard–Jones potential. The collision integral can be found with Eq. (13). M_{H_2} and M_{H_2O} are the molecular weight of hydrogen and water. The average energy well depth is calculated with $\in_{H_2-H_2O} = (\in_{H_2}\in_{H_2O})^{0.5}$ in ergs. $\in_{H_2}$ and $\in_{H_2O}$ are found from the viscosity of the gas [33]. The average collision diameter is calculated with $\sigma_{H_2-H_2O} = \frac{\sigma_{H_2}+\sigma_{H_2O}}{2}$. σ_{H_2} and σ_{H_2O} are the collision diameters of the specie molecules in
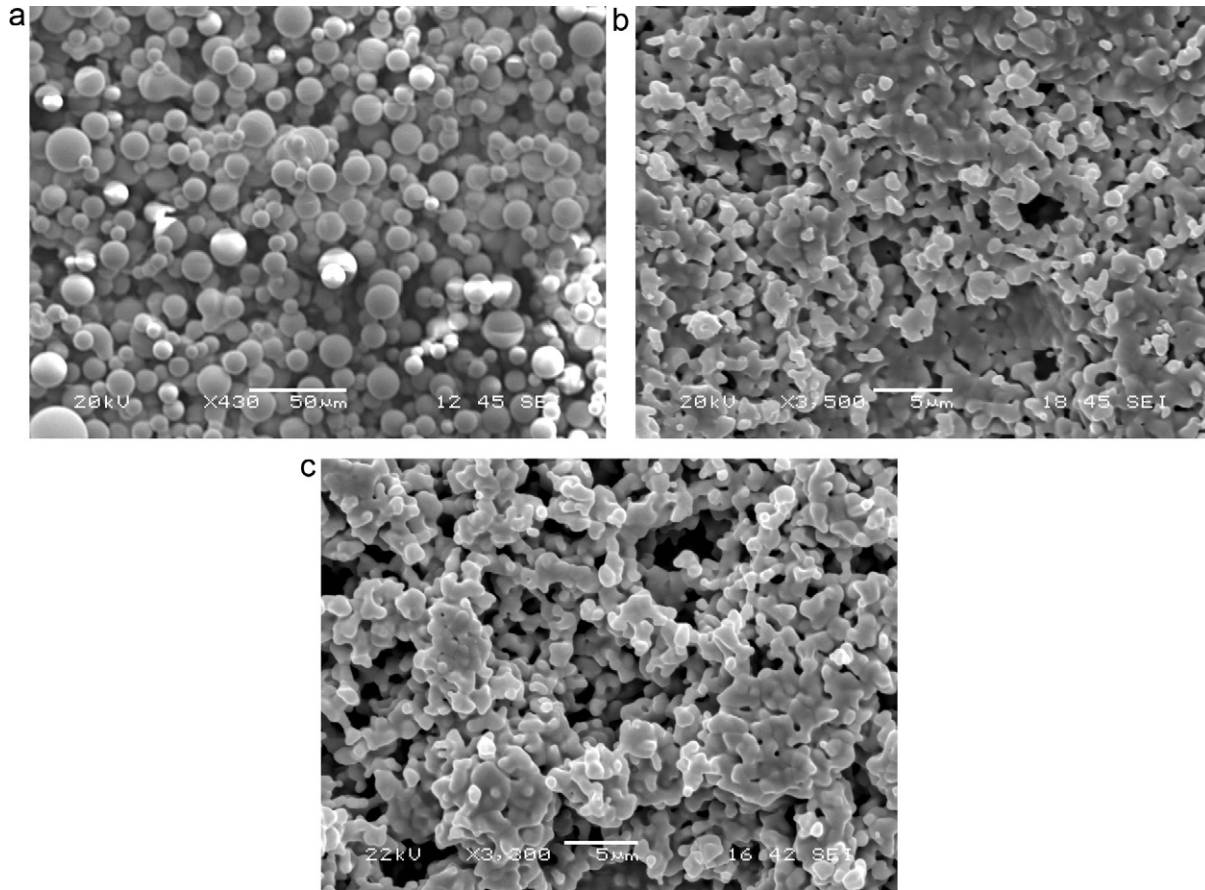
Fig. 3. SEM images of anode microstructures: (a) Sample #1 ($d_p = 17$ μm, $\varepsilon = 36\%$), (b) Sample #2 ($d_p = 2.5$ μm, $\varepsilon = 22\%$) and (c) Sample #3 ($d_p = 1.5$ μm, $\varepsilon = 34\%$).

angstroms [34].

$$D_{H_2-H_2O} = 0.0018583 \left(\frac{1}{M_{H_2}} + \frac{1}{M_{H_2O}} \right)^{1/2} \frac{T^{1.5}}{p_a \sigma_{H_2-H_2O}^2 \Omega_{D,H_2-H_2O}} \quad (12)$$

$$\Omega_{D,H_2-H_2O} = \frac{A}{(T^*)^B} + \frac{C}{\exp(DT^*)} + \frac{E}{\exp(FT^*)} + \frac{G}{\exp(HT^*)} \quad (13)$$

where $T^* = KT/ \in_{H_2-H_2O}$, $A = 1.06036$, $B = 0.15610$, $C = 0.19300$, $D = 0.47635$, $E = 1.03587$, $F = 1.52996$, $G = 1.76474$, $H = 3.89411$.

The Knudsen diffusion coefficient can be calculated with Eq. (14) [12,35] for gas specie A, where d_{pore} is the diameter of the pore.

$$D_{AK} = 48.5 d_{pore} \sqrt{\frac{T}{M_A}} \quad (14)$$

The effective diffusion coefficient can be found with Eq. (15), where ε and τ represent porosity and tortuosity of the porous structure.

$$D_{A(eff)} = \frac{\varepsilon}{\tau} \left(\frac{1}{D_{AB}} + \frac{1}{D_{AK}} \right)^{-1} \quad (15)$$

where tortuosity τ can be estimated using the model described in [36].

The micro model was developed by Costamagna et al. [26] based on the theory of random packed spheres to describe electrode microstructure. The micro model considers parameters, which includes porosity, particle size, particle coordination number, electronic-ionic conductor size ratio, electronic-ionic conductor particle number fraction, and bulk material conductivities. The model then outputs effective resistivity and pore size, which are transferred to the macro model to calculate the Ohmic loss and the concentration loss.

The spheres are a binary mixture of electronic and ionic conducting particles with a contact angle between them to account for sintering. In this model, the parameter R_p was defined as the ratio of ionic conducting particles as the matrix to the electronic conducting particles, as seen in Eq. (16).

$$R_p = \frac{r_{io}}{r_{el}} \quad (16)$$

The mixture of binary particles has the following coordination number based on the particle type as seen in Eq. (17). The coordination number Z equals 6 in a random packing sphere system, and n_{el} and n_{io} are the number fraction of electronic and ionic conducting particles.

$$Z_{el} = 3 + \frac{Z-3}{n_{el} + (1-n_{el})R_p^2} \quad \text{and} \quad Z_{io} = 3 + \frac{(Z-3)R_p^2}{n_{io} + (1-n_{io})R_p^2} \quad (17)$$

The volume fraction can be found from the R_p ratio and the number fraction of conducting particles of that phase as seen in Eq. (18).

$$\varphi_{el} = \frac{n_{el}}{n_{el} + (1-n_{el})R_p^3} \quad \text{and} \quad \varphi_{io} = \frac{n_{io}}{n_{io} + (1-n_{io})R_p^{-3}} \quad (18)$$

The chance of electrical or ionic percolation occurring is based upon the probability of a continuous cluster of conducting particles from the electrolyte to the electrode free surface existing in the electrode. Costamagna et al. used Eq. (19), developed by Bouvard, modifying the coefficients based on the experimental
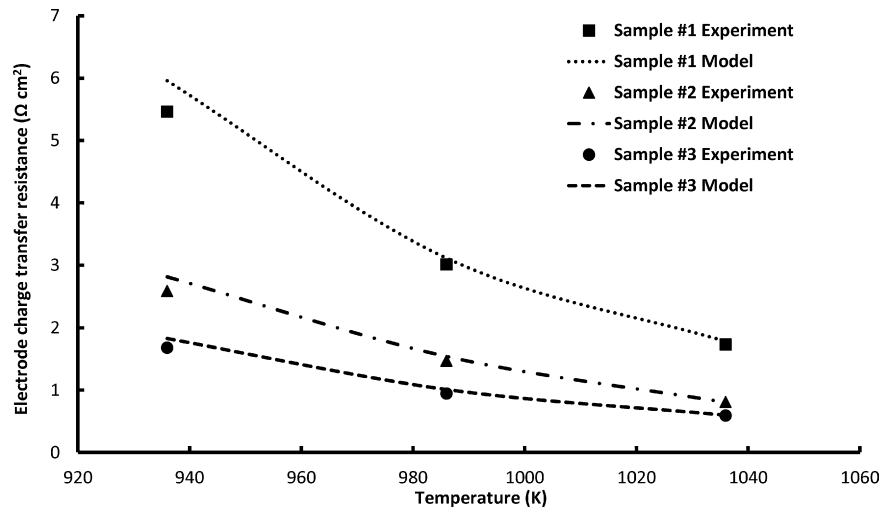
Fig. 4. Model validation with electrochemical impedance spectroscopy experiment results.

determination of $Z_{m-m} = 1.764$ by Kuo and Gupta [37]. Subscript m denotes the particle conducting phase.

$$p_m = \left(1 - \left(\frac{4.236 - Z_{m-m}}{2.472}\right)^{2.5}\right)^{0.4} \qquad (19)$$

It was shown that Suzuki's model was accurate for $0.154 < R_p < 6.464$. Suzuki's model utilized Eq. (20) [38].

$$Z_{el-el} = \frac{n_{el}Z}{n_{el} + (1 - n_{el})R_p^2} \quad \text{and} \quad Z_{io-io} = \frac{n_{io}Z}{n_{io} + (1 - n_{io})R_p^{-2}} \qquad (20)$$

The number of particles per unit volume n_t can be calculated with Eq. (21). Eqs. (21) and (22) are used when $R_p > 1$.

$$n_t = \frac{1 - \varepsilon}{(4/3)\pi r_{el}^3 (n_{el} + (1 - n_{el})R_p^3)} \qquad (21)$$

The area of TPB A between the spheres per volume can be calculated with Eq. (22). θ is the contact angle of the smaller particle.

$$A = \frac{\pi (r_{el} \sin(\theta_{el}))^2 n_t n_{el} n_{io} Z_{el} Z_{io} p_{el} p_{io}}{Z} \qquad (22)$$
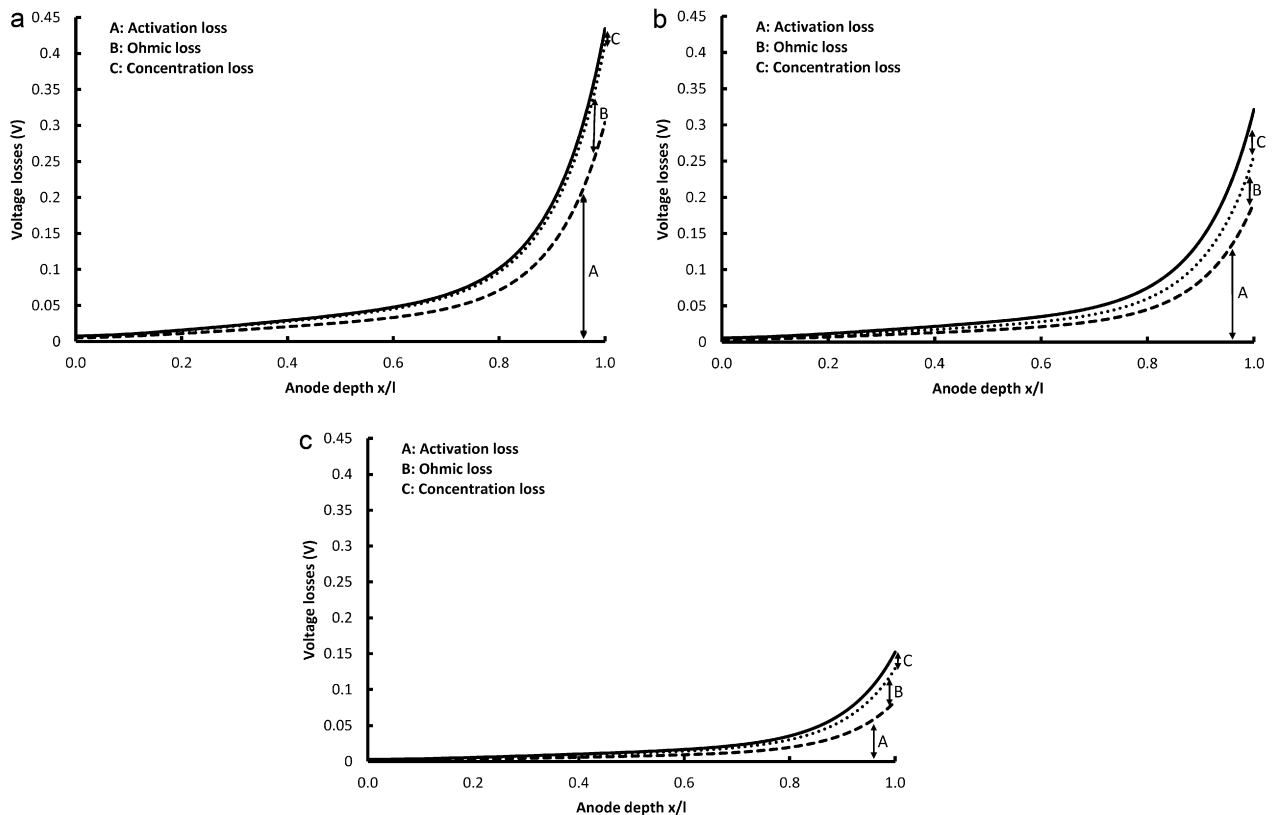

Fig. 5. Voltage loss distribution: (a) Sample #1, (b) Sample #2 and (c) Sample #3.

Table 1
Boundary conditions for the anode.

$x = 0$ (free surface)	$\frac{dV_{loss}}{dx} = \rho_{el(eff)}i_{el}$ and $i_{el} = I_t$ $p_{H_2} = p_{H_2}^i$
$x = l$ (interface between electrode and electrolyte)	$\frac{dV_{loss}}{dx} = \rho_{io(eff)}i_{io}$

If $R_p < 1$, then Eqs. (23) and (24) should be utilized. Notice that θ is based on the smaller particle. If $R_p = 1$, then either equation set can be used.

$$n_t = \frac{1 - \varepsilon}{(4/3)\pi r_{io}^3(n_{io} + (1 - n_{io})R_p^{-3})} \tag{23}$$

$$A = \frac{\pi(r_{io}\sin(\theta_{io}))^2 n_t n_{el} n_{io} Z_{el} Z_{io} p_{el} p_{io}}{Z} \tag{24}$$

The effective resistivity can be calculated using Eq. (25), rewritten from Costamagna et al. [26]. γ is the necking factor between the contacting particles, and $\gamma = 0.5$ is commonly accepted value [12,26]. The critical number fraction is obtained from percolation theory critical thresholds for a randomly packed bimodal spheres [22,35,39].

$$\rho_{el(eff)} = \frac{(1 - n_{el,cr})^2}{\gamma\sigma_{el}(n_{el} - n_{el,cr})^2} \quad \text{and} \quad \rho_{io(eff)} = \frac{(1 - n_{io,cr})^2}{\gamma\sigma_{io}(n_{io} - n_{io,cr})^2} \tag{25}$$

Pore diameter can be calculated from Eq. (26) [40].

$$d_{pore} = \frac{2}{3}\frac{d_{el}\varepsilon}{(1 - \varepsilon)}\frac{n_{el} + (1 - n_{el})R_p^3}{n_{el} + (1 - n_{el})R_p^2} \tag{26}$$

The second-order derivative of total voltage loss can be expressed as Eq. (27) using Butler–Volmer equation coupled with mass transport equation [12,15,26]. By combining Eqs. (5)–(7), (10) and (11), the system of coupled differential equations that is used for the anode can be represented as Eqs. (27)–(29). p_a is the total pressure on anode, and $p_a = p_{r,H_2} + p_{r,H_2O}$. Eqs. (27)–(29) can be easily modified and used for the cathode as well.

$$\frac{d^2V_{loss}}{dx^2} = (\rho_{el(eff)} + \rho_{io(eff)})Ai_o\left[\frac{p_{r,H_2}}{p_{H_2}^i}\exp\left(\frac{\beta nFV_{loss}}{RT}\right)\right.$$
$$\left. - \frac{p_a - p_{r,H_2}}{p_a - p_{H_2}^i}\exp\left(-(1-\beta)\frac{nFV_{loss}}{RT}\right)\right] \tag{27}$$

$$\frac{dp_{r,H_2}}{dx} = -\frac{RT}{2F}\frac{i_{el}}{(1 - (p_{r,H_2}/p_a))D_{H_2(eff)} + (p_{r,H_2}/p_a)D_{H_2O_{(eff)}}} \tag{28}$$

$$\frac{di_{el}}{dx} = -Ai_o\left[\frac{p_{r,H_2}}{p_{H_2}^i}\exp\left(\frac{\beta nFV_{loss}}{RT}\right)\right.$$
$$\left. - \frac{p_a - p_{r,H_2}}{p_a - p_{H_2}^i}\exp\left(-(1-\beta)\frac{nFV_{loss}}{RT}\right)\right] \tag{29}$$

The boundary conditions for this coupled, boundary value equation system are summarized in Table 1.

After the distribution of total voltage loss is calculated, the overall electrode charge transfer resistance can be determined.

$$R_{ct} = \frac{V_{loss}}{I_t} \tag{30}$$

where I_t is the total current density in the electrode.

Table 2
Values of model parameters used in validation.

Model parameter	Value
Anode thickness (μm)	150
YSZ/Ni volume fractions (unitless) [41]	0.17/0.21
Electronic particle diameter (μm) [41]	1.28
Ionic particle diameter (μm) [41]	0.1
Porosity (unitless)	0.3
Tortuosity (unitless) [15,26]	4.5
Necking factor (unitless) [26]	0.5
Hydrogen supply pressure (Pa) [12]	98,261
Anode electronic conductivity (S m^{-1}) [12]	2×10^6
Anode ionic conductivity, YSZ (S m^{-1}) [48]	$2.706 \times 10^6 \exp(-0.64/(8.617 \times 10^{-5}T))/T$

3. Results and discussion

The developed model was validated against experimental work by Jiang et al. [41]. The model parameters used for the validation are shown in Table 2. Fig. 2(a) and (b) shows Jiang et al's [41] experimental data with the fitted model curves. It can be seen that a reasonable fit was obtained for both YSZ doping levels and both operating temperatures. The exchange current density was the only fitting parameter used and was between 1000 A m^{-2} and 6500 A m^{-2}. These values are reasonable when compared with those found in the literatures [12,42,43]. In the validated model, actual electronic and ionic particle sizes reported in Jiang et al's
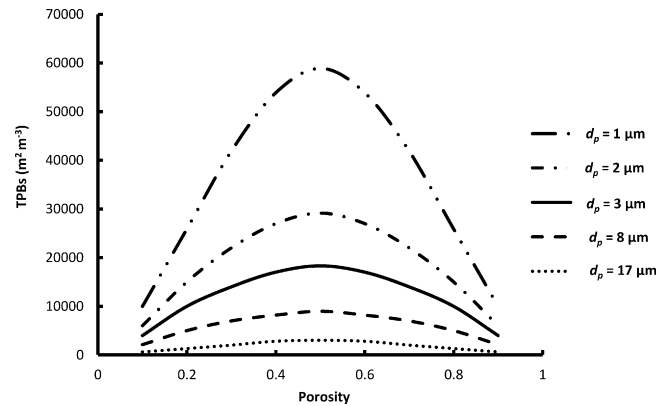

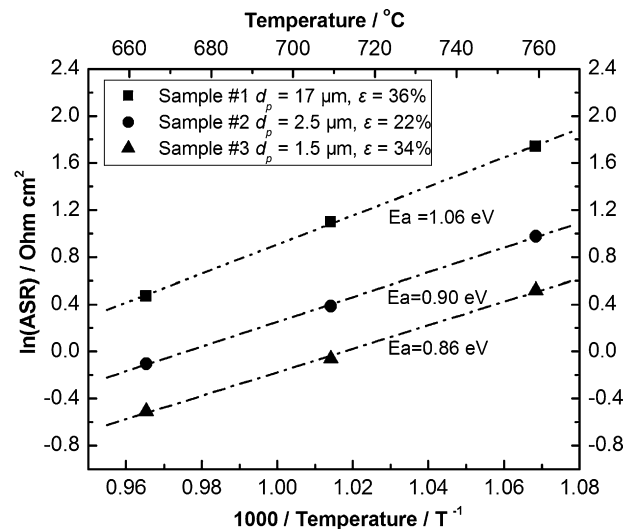**Fig. 6.** TPB reaction area versus electrode particle size.

Fig. 7. Nyquist plots depicting EIS results for various samples at three test temperatures.
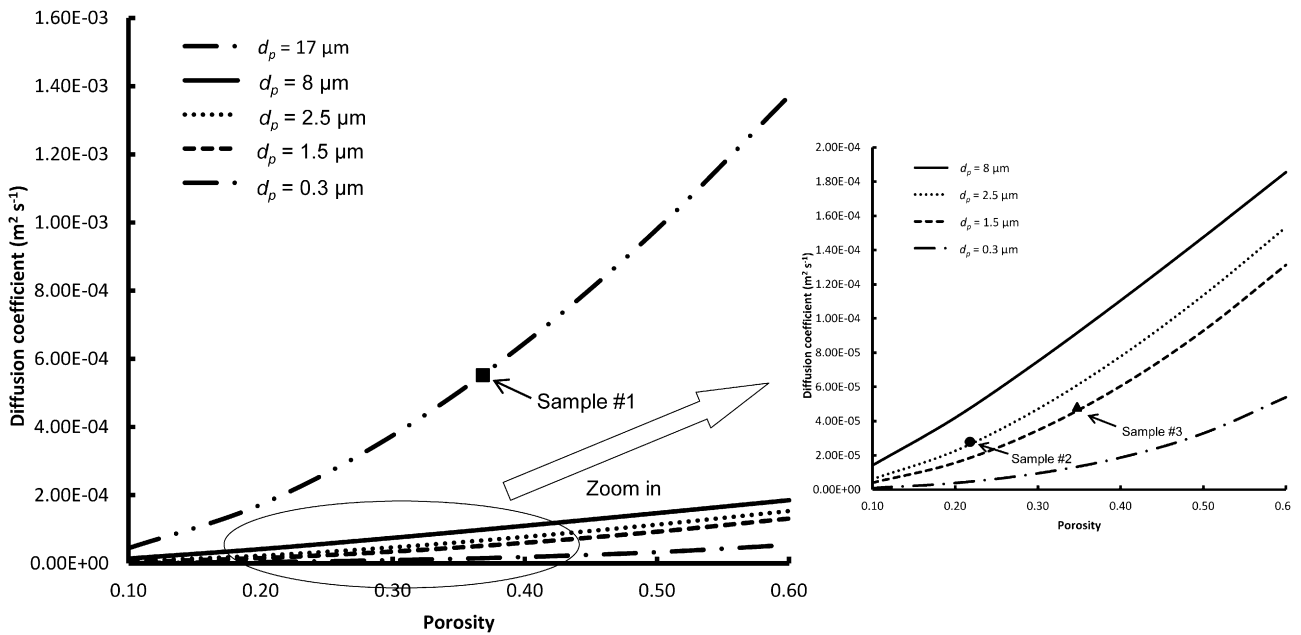
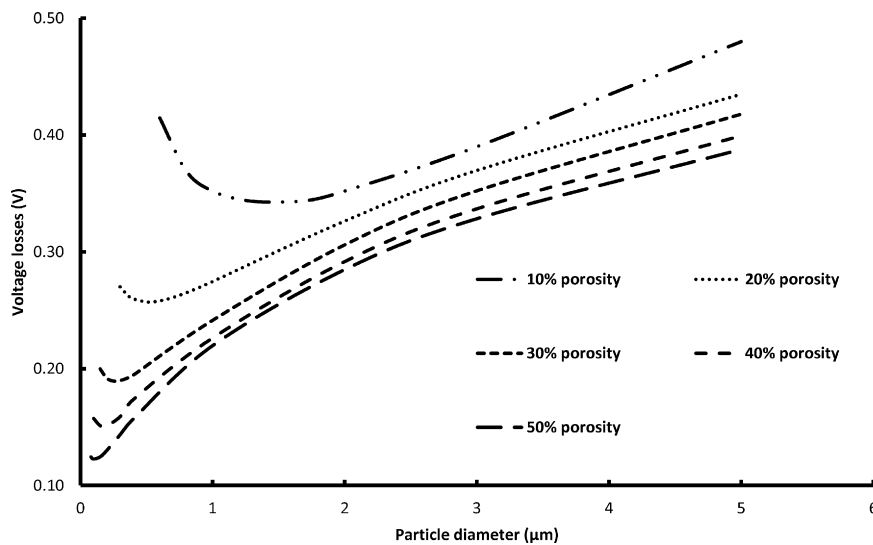**Fig. 8.** Diffusion coefficients for three test samples.

Fig. 9. Voltage losses with different porosity and particle size in homogeneous SOFC electrode.

work were used. Images of their electrochemical impedance spectroscopy measurement suggested that the cell may have suffered significant concentration loss. Therefore, the tortuosity used for fitting the experimental data was larger than those commonly accepted values for structures with porosity around 30%. The contribution of each voltage loss terms are separately plotted in Fig. 2(b). The diffusion loss accounts for about 30% of total losses, which may likely occur in an anode-supported SOFC with thick catalyst doping.

The developed model was also validated against experiments conducted by the authors. Three different nickel–Ce0.9Gd0.1O1.95 (Ni–CGO) anodes were prepared on a dense yttria stabilized zirconia (YSZ) substrate by ultrasonic spray pyrolysis. The detailed description of the experimental procedure and electrochemical impedance spectroscopy measurement can be found in the authors' previous studies [22,39]. Sample preparation conditions, microstructure details and morphology are listed and shown in Table 3 and Fig. 3. Model parameters used in the validation and

Table 3
Test sample preparation condition and sample microstructure information.

#	Precursor solution concentration C (mol l^{-1})	Deposition temperature T (K)	Average deposition particle size d_p (μm)	Deposited film porosity ε (%)	Deposited film thickness l (μm)
1	0.4	523	17	36	37
2	0.025	523	2.5	22	23
3	0.025	623	1.5	34	18

Precursor solution feed rate fixed as 1.23 ml min^{-1}.

Table 4
Model parameters and validation.

| Test sample #	Test temperature (K)	Electrode charge transfer resistance ($\Omega\,cm^2$) experiment	Electrode charge transfer resistance ($\Omega\,cm^2$) model	Discrepancy (%)
(a) Model validation with experimental results				
1	1036	1.731	1.780	2.83
1	986	3.011	3.114	3.42
1	936	5.460	5.958	9.12
2	1036	0.808	0.803	0.62
2	986	1.469	1.540	4.83
2	936	2.587	2.813	8.74
3	1036	0.591	0.597	1.02
3	986	0.944	1.010	7.00
3	936	1.678	1.826	8.82

Model parameter		Value
(b) Values of model parameters used in validation		
Temperature (K)	T	1036/986/936
Total pressure on anode (Pa)	p_a	101,300
Pressure of hydrogen (Pa) [12]	$p_{H_2}^i$	86,105
Pressure of oxygen (Pa)	$p_{H_2O}^i$	21,273
Electronic number fraction (unitless)	n_{el}	(#1) 0.384/(#2) 0.468/(#3) 0.396
Ionic number fraction (unitless)	n_{io}	(#1) 0.256/(#2) 0.312/(#3) 0.264
Exchange current density of anode ($A\,m^{-2}$)	$i_{o(a)}$	(#1) 2375/(#2) 4500/(#3) 4735
Thickness of anode (μm)	l	(#1) 37/(#2) 23/(#3) 18
Electronic conductor in anode ($S\,m^{-1}$) $\times 10^6$ [49]	σ_{el}	5.31@1036 K/5.16@986/5.08@936
Ionic conductor in anode ($S\,m^{-1}$) [48]	σ_{io}	$2.706 \times 10^6 \exp(-0.64/(8.6173 \times 10^{-5}T))/T$
Porosity (unitless)	ε	(#1) 0.36/(#2) 0.22/(#3) 0.34
Tortuosity (unitless) [36]	τ	(#1) 1.9/(#2) 4/(#3) 2.0
Number of electrons in reaction (unitless) [29–31]	n	1
Necking factor (unitless) [26]	γ	0.5
Symmetry factor (unitless) [12,15,50,51]	β	0.5
Faraday's constant ($C\,mol^{-1}$)	F	96,485
Gas constant ($J\,(mol\,K)^{-1}$)	R	8.314

results are summarized in Table 4 and plotted in Fig. 4. The model prediction agrees well with the experimental results with discrepancy smaller than 10%.

Three test samples with different homogenous microstructures were analyzed to evaluate their electrochemical performance using the developed model. Fig. 5 shows the voltage loss distribution of the three different test samples. Activation loss, Ohmic loss and concentration loss were separated from the total voltage loss. The activation loss is the most dominant loss, which is related to the TPB area and activation energy. When the electrode particle size decreases, the TPB area dramatically increases based on Eq. (22), as shown in Fig. 6. It is known that the decrease in particle size increases the TPB, and thereby, improves the performance of deposited electrodes [44]. This improvement in electrode performance is clearly seen here, where the charge transfer resistance decreased from 5.45 $\Omega\,cm^2$ for Sample #1 to 0.61 $\Omega\,cm^2$ for Sample #3 at 663 °C. Notably, these resistance values are within the typical range reported in the literature [45–47].

The temperature dependent electrode charge transfer resistances that were measured could be used to determine the activation energy (E_a) of the different electrodes. The activation energies as determined from the impedance test are provided in the Arrhenius plot in Fig. 7. A decrease in the activation energy is observed when comparing Samples #1, #2 and #3. The decrease in the activation energy reduces the activation loss and its percentage of total voltage losses in those three samples, as shown in Fig. 4. High diffusion capability also plays an important role in improving the SOFC performance. It can be seen from Fig. 8 that diffusion coefficients, which account for concentration loss, vary dramatically with different electrode particle sizes. The diffusion coefficient can be increased by adopting a larger electrode particle size. With similar electrode particle size, highly porous structure helps to obtain high gas diffusion capability.

Fig. 9 shows the relationship between voltage loss and particle size for six different porosities from 10% to 50% at 12,000 $A\,m^{-2}$. All curves display optimal particle size that minimizes the voltage loss given the porosity. The particle size at the minimum voltage losses for each porous homogenous anode structure increases with decreasing porosity. By increasing the porosity, the voltage losses decrease. For all curves, diffusion losses are dominant left to the optimal particle size and activation losses are dominant right to the optimal particle size. The best performance occurs when the particle size is small and porosity is high although such structure is limited by the mechanical failure. Based on the findings of our previous thermo-mechanical model [11], as seen in
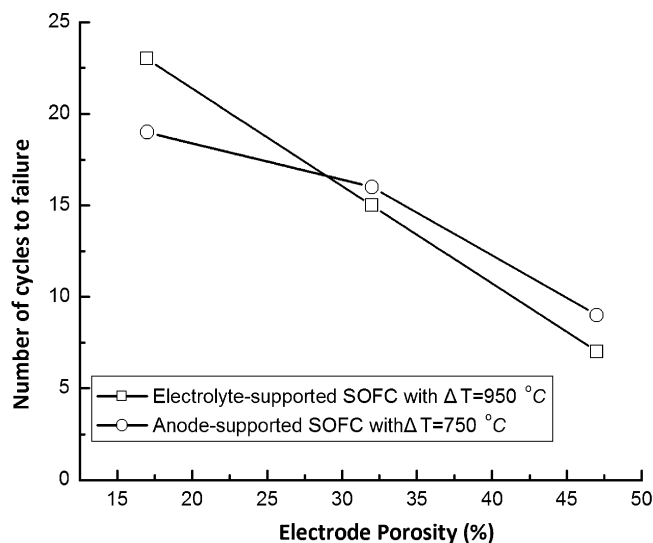
Fig. 10. Cell life variation at different electrode porosities.

Fig. 10, the lifetime of a cell decreases with increasing porosity. From the standpoint of structural reliability, high porous structure over 50% should be avoided. Therefore, the optimization analysis of cell structure should be carried out not only from the electrochemical performance standpoint, but also consider the structural reliability.

4. Conclusion

In this paper, a numerical analysis has been performed to evaluate the effects of electrode microstructure variation on the SOFC performance. The modeling was achieved by integrating a macro model and a micro model. The macro model describes the overall cell behavior through activation, Ohmic, and concentration losses based on chemical and concentration potentials. The micro model, which considers the electrode microstructural parameters (electrode effective conductivity, TPB area and pore size), is integrated into the macro model. Numerical results were validated against other's and our own experimental results, which were within 10% of experimentally measured results. Analysis on the contribution of each major voltage loss showed that the activation loss was the most significant, which was relates to the TPB area and activation energy. The developed model could be used as a tool to effectively analyze and evaluate the electrochemical performance of a designed SOFC electrode. Overall, the experimental and numerical analysis demonstrated the potential of controlling the electrode microstructure of a SOFC to improve the electrochemical performance of a cell. It is suggested that the optimization of the SOFC microstructure and performance should be carried out considering not only the electrochemical performance, but also structure reliability. In the future, the developed thermo-mechanical model and proposed electrochemical model will be integrated to a full scale multiphysics model.

References

[1] Fuel Cell Handbook, 7th ed., EG&G Technical Services Inc., Morgantown, WV, 2004.
[2] S.J. Litzelman, J.L. Hertz, W. Jung, H.L. Tuller, Fuel Cells 8 (2008) 294–302.
[3] Y. Zhao, N. Shah, N. Brandon, Fuel Cells 10 (2010) 181–193.
[4] F.N. Cayan, M. Zhi, S.R. Pakalapati, I. Celik, N. Wu, R. Gemmen, J. Power Sources 185 (2008) 595–602.
[5] S. Ma, J. Wang, Z. Yan, Y. Dai, B. Lu, J. Power Sources 196 (2011) 8463–8471.
[6] F.P. Nagel, T.J. Schildhauer, J. Sfeir, A. Schuler, S.M.A. Biollaz, J. Power Sources 189 (2009) 1127–1131.
[7] W.A. Surdoval, 7th SECA Public Workshop & Peer Review, Philadelphia, 2006.
[8] S. Shaffer, Development Update on Delphi's Solid Oxide Fuel Cell Power System, Electrochemical Society Inc., Philadelphia, PA, 2006.
[9] M. Ni, M.K.H. Leung, D.Y.C. Leung, Fuel Cells 7 (2007) 269–278.
[10] K.N. Grew, A.S. Joshi, W.K.S. Chiu, Fuel Cells 10 (2010) 1143–1156.
[11] L. Liu, G.-Y. Kim, A. Chandra, J. Power Sources 195 (2010) 2310–2318.
[12] S.H. Chan, Z.T. Xia, J. Electrochem. Soc. 148 (2001) A388–A394.
[13] L. Zhao, B. He, J. Gu, F. Liu, X. Chu, C. Xia, Int. J. Hydrogen Energy (2011).
[14] R. O'Hayre, D.M. Barnett, F.B. Prinz, J. Electrochem. Soc. 152 (2005) 439–444.
[15] M. Ni, M.K.H. Leung, D.Y.C. Leung, J. Power Sources 168 (2007) 369–378.
[16] P. Holtappels, C. Bagger, J. Eur. Ceram. Soc. 22 (2002) 41–48.
[17] S.P. Jiang, J. Power Sources 124 (2003) 390–402.
[18] A. Barbucci, R. Bozzo, G. Cerisola, P. Costamagna, Electrochim. Acta 47 (2002) 2183–2188.
[19] J.H. Lee, H. Moon, H.W. Lee, J. Kim, J.D. Kim, K.H. Yoon, Solid State Ionics 148 (2002) 15–26.
[20] S.-D. Kim, J.-J. Lee, H. Moon, S.-H. Hyun, J. Moon, J. Kim, H.-W. Lee, J. Power Sources 169 (2007) 265–270.
[21] P. Holtappels, C. Sorof, M.C. Verbraeken, S. Rambert, U. Vogt, Fuel Cells 6 (2006) 113–116.
[22] L. Liu, G.-Y. Kim, A.C. Hillier, A. Chandra, J. Power Sources 196 (2011) 3026–3032.
[23] E.S. Greene, W.K.S. Chiu, M.G. Medeiros, J. Power Sources 161 (2006) 225–231.
[24] J. Deseure, L. Dessemond, Y. Bultel, E. Siebert, J. Eur. Ceram. Soc. 25 (2005) 2673–2676.
[25] L.C.R. Schneider, C.L. Martin, Y. Bultel, L. Dessemond, D. Bouvard, Electrochim. Acta 52 (2007) 3190–3198.
[26] P. Costamagna, P. Costa, V. Antonucci, Electrochim. Acta 43 (1998) 375–394.
[27] C.O. Colpan, I. Dincer, F. Hamdullahpur, Int. J. Energ. Res. 32 (2008) 336–355.
[28] P. Aguiar, C.S. Adjiman, N.P. Brandon, J. Power Sources 138 (2004) 120–136.
[29] K.J. Yoon, P. Zink, S. Gopalan, U.B. Pal, J. Power Sources 172 (2007) 39–49.
[30] H. Zhu, R.J. Kee, J. Power Sources 117 (2003) 61–74.
[31] D.A. Noren, M.A. Hoffman, J. Power Sources 152 (2005) 175–181.
[32] S.H. Chan, K.A. Khor, Z.T. Xia, J. Power Sources 93 (2001) 130–140.
[33] E.L. Cussler, Diffusion Mass Transfer in Fluid Systems, Cambridge University Press, New York, 1984.
[34] R.C. Reid, J.M. Prausnitz, B.E. Poling, The Properties of Gases & Liquids, 4th ed., McGraw-Hill Book Company, New York, 1987.
[35] R.N.M. Anthony, L. Hines, Mass Transfer: Fundamentals and Applications, Prentice-Hall, Englewood Cliffs, NJ, 1985.
[36] P.Y. Lanfrey, Z.V. Kuzeljevic, M.P. Dudukovic, Chem. Eng. Sci. 65 (2010) 1891–1896.
[37] C.H. Kuo, P.K. Gupta, Acta Metall. Mater. 43 (1995) 397–403.
[38] M. Suzuki, T. Oshima, Powder Technol. 35 (1983) 159–166.
[39] L. Liu, G.-Y. Kim, A. Chandra, J. Power Sources 195 (2010) 7046–7053.
[40] J.H. Nam, D.H. Jeon, Electrochim. Acta 51 (2006) 3446–3460.
[41] S.P. Jiang, W. Wang, Y.D. Zhen, J. Power Sources 147 (2005) 1–7.
[42] A.V. Virkar, J. Chen, C.W. Tanner, J.W. Kim, Solid State Ionics 131 (2000) 189–198.
[43] F. Zhao, A.V. Virkar, J. Power Sources 141 (2005) 79–95.
[44] C.-X. Li, C.-J. Li, L.-J. Guo, Int. J. Hydrogen Energy 35 (2010) 2964–2969.
[45] U.P. Muecke, K. Akiba, A. Infortuna, T. Salkus, N.V. Stus, L.J. Gauckler, Solid State Ionics 178 (2008) 1762–1768.
[46] S. Primdahl, Y.L. Liu, J. Electrochem. Soc. 149 (2002) A1466–A1472.
[47] T. Ishihara, T. Shibayama, H. Nishiguchi, Y. Takita, Solid State Ionics 132 (2000) 209–216.
[48] R.T. Leah, N.P. Brandon, P. Aguiar, J. Power Sources 145 (2005) 336–352.
[49] V. Gil, C. Moure, J. Tartaj, J. Eur. Ceram. Soc. 27 (2007) 4205–4209.
[50] C.B. Lee, J.M. Bae, J. Power Sources 176 (2008) 62–69.
[51] J.W. Kim, A.V. Virkar, K.Z. Fung, K. Mehta, S.C. Singhal, J. Electrochem. Soc. 146 (1999) 69–78.